Intermittent Intense Turbulent Mixing under Ice in the Laptev Sea Continental Shelf

YUENG-DJERN LENN, TOM P. RIPPETH, AND CHRIS P. OLD

School of Ocean Sciences, Bangor University, Menai Bridge, United Kingdom

SHELDON BACON

National Oceanography Centre, Southampton, United Kingdom

IGOR POLYAKOV

International Arctic Research Center, University of Alaska Fairbanks, Fairbanks, Alaska

VLADIMIR IVANOV

International Arctic Research Center, University of Alaska Fairbanks, Fairbanks, Alaska, and Scottish Association for Marine Science, Oban, United Kingdom, and Arctic and Antarctic Research Institute, St. Petersburg, Russia

JENS HÖLEMANN

Alfred Wegener Institute, Bremerhaven, Germany

(Manuscript received 7 January 2010, in final form 5 November 2010)

ABSTRACT

Vertical mixing in the bottom boundary layer and pycnocline of the Laptev Sea is evaluated from a rapidly sampled 12-h time series of microstructure temperature, conductivity, and shear observations collected under 100% sea ice during October 2008. The bottom boundary turbulent kinetic energy dissipation was observed to be enhanced ($\epsilon \sim 10^{-4}$ W m^{-3}) beyond background levels ($\epsilon \sim 10^{-6}$ W m^{-3}), extending up to 10 m above the seabed when simulated tidal currents were directed on slope. Upward heat fluxes into the halocline-class waters along the Laptev Sea seabed peaked at ~4–8 W m^{-2}, averaging out to ~2 W m^{-2} over the 12-h sampling period. In the Laptev Sea pycnocline, an isolated 2-h episode of intense dissipation ($\epsilon \sim 10^{-3}$ W m^{-3}) and vertical diffusivities was observed that was not due to a localized wind event. Observations from an acoustic Doppler current meter moored in the central Laptev Sea near the M_2 critical latitude are consistent with a previous model in which mixing episodes are driven by an enhancement of the pycnocline shear resulting from the alignment of the rotating pycnocline shear vector with the under-ice stress vector. Upward cross-pycnocline heat fluxes from the Arctic halocline peaked at ~54 W m^{-2}, resulting in a 12-h average of ~12 W m^{-2}. These results highlight the intermittent nature of Arctic shelf sea mixing processes and how these processes can impact the transformation of Arctic Ocean water masses. The observations also clearly demonstrate that absence or presence of sea ice profoundly affects the availability of near-inertial kinetic energy to drive vertical mixing on the Arctic shelves.

1. Introduction

The Arctic Ocean is characterized by a cold fresh halocline which separates and insulates the colder and fresher surface polar mixed layer (PML) from warmer saltier water of Atlantic or Pacific origin at intermediate depths (e.g., Aagaard et al. 1981; Rudels et al. 1996; Meincke et al. 1997). The Arctic halocline is thought to be formed and maintained by an influx to the polar basins of cold saline water formed during freezing on the Arctic continental shelf seas (Aagaard et al. 1981). Consequently, Arctic halocline formation theories have focused on mechanisms for diapycnal and lateral mixing of the shelf and oceanic waters (e.g., Rudels et al. 2000; Woodgate et al. 2005; Shimada et al. 2005; Itoh et al. 2007). These

Corresponding author address: Yueng-Djern Lenn, School of Ocean Sciences, Bangor University, Menai Bridge, Anglesey LL59 5AB, United Kingdom.
E-mail: y.lenn@bangor.ac.uk

DOI: 10.1175/2010JPO4425.1

© 2011 American Meteorological Society

halocline formation and maintenance mechanisms are critical to Arctic upper-ocean stratification that in turn influences Arctic circulation, sea ice, and climate.

Mixing between the different water masses during halocline formation is unlikely to occur in the Arctic interior, where the observed turbulent kinetic energy is weak (e.g., Padman 1995; Rainville and Winsor 2008; Fer 2009). From the few observations available, mixing along the Arctic Ocean periphery appears to be inhomogeneous. Near the Yermak Plateau, the internal wave field has been observed to be significantly elevated over Arctic interior levels and can provide energy for turbulent mixing (Padman and Dillon 1991; Padman et al. 1992; D'Asaro and Morison 1992; Fer et al. 2010). Marked variability exists even in this small region, where Fer et al. (2010) observed stronger stratification and weaker diffusivities suppressing mixing on the south side of the Yermak Plateau relative to the north side. This results in small AW heat loss (2–4 W m^{-2}) when the West Spitsbergen Current traverses the southern flank of the Yermak Plateau, in comparison to higher AW heat losses (15 W m^{-2}) when the current traverses the Plateau's northern flank.

Away from the complicated submarine topography of the Yermak Plateau, Arctic boundary mixing can be as weak as the interior basins. North of the Laptev and East Siberian Seas, recent observations in the Arctic boundary current showed that the vertical mixing in the upper thermocline is weak and dominated by double diffusion rather than turbulent diapycnal mixing (Lenn et al. 2009). The resulting vertical heat fluxes ($\leq$1 W m^{-2}) through the upper thermocline are an order of magnitude too small to account for the halocline and AW cooling observed between adjacent cross sections of the Arctic boundary current (Lenn et al. 2009). This implies that lateral exchange with the more energetic shelf seas may be more important (Turner 2010).

The importance of vertical mixing due to the dissipation of wind or tidal energy has been well documented in ice-free continental shelf seas and estuaries (e.g., Simpson et al. 1996; Mackinnon and Gregg 2005; Rippeth 2005; Burchard and Rippeth 2009, hereafter BR09). In moored current observations from the Chukchi Sea continental shelf in the western Arctic, Rainville and Woodgate (2009) found a pronounced seasonal signal in wind-driven inertial shear, implying vertical mixing, correlated with the annual cycle of sea ice concentration. Tides provide direct forcing to the Arctic marginal seas in all seasons. Recent observations and numerical models suggest that strong internal tides are present in the Kara and Barents Seas and could provide energy for turbulent mixing (Sundfjord et al. 2007; Morozov et al. 2008; Sirevaag and Fer 2009). By introducing parameterizations for tidal mixing to a pan-Arctic coupled ice–ocean model, Holloway and Proshutinsky (2007) presented persuasive evidence that tidal mixing in the Arctic seas, particularly over and near the continental slope, is essential for the AW modification and setting Arctic Ocean stratification. Despite their importance to Arctic halocline formation and potential consequences for Arctic circulation and climate, we have yet to identify specific tidal mixing processes that dominate the Arctic shelf sea environments and quantify their effect.

In this study, we investigate the tidally driven mixing in the Arctic shelf seas with new rapidly sampled time-series observations of turbulent dissipation and water column stratification in the north Laptev Sea (NLS). These new hydrographic and microstructure shear, temperature, and conductivity observations resolve the bottom boundary dissipation associated with the dominant semidiurnal M_2 tide, as well as an unexpected isolated episode of intense mixing in the pycnocline located at base of the PML. Additional moored current velocity observations from the central Laptev Sea and barotropic tide predictions provide insight on the possible causes of the observed pycnocline mixing. The study is laid out as follows: section 2 contains descriptions of the observations, tide model, analytical methods, and hydrographic environment; section 3 focuses on boundary layer mixing observed in the NLS; section 4 describes the observations of intense pycnocline mixing in the NLS and pycnocline shear variability in the central Laptev Sea (CLS); section 5 includes a discussion of the mechanisms driving intermittent shear enhancement and mixing, as well as the consequences of the observed vertical fluxes; and section 6 summarizes our conclusions.

2. Data, environment, and methods

a. North Laptev Sea observations

The 2008 Arctic Basin-wide Synoptic Oceanography (ASBO) field season was undertaken as a joint cruise with the Nansen and Amundsen Basins Observational System (NABOS) research program aboard the Russian icebreaking vessel I/B *Kapitan Dranitsyn*. On 12 October 2008, a microstructure dissipation time series was collected over a 12-h period in the northern Laptev Sea. The data were collected under 100% ice coverage of a first-year ice sheet ~1 m thick, at a mean position of 79°14.81′N, 144°56.13′E and a nominal water depth of 100 m (Fig. 1). The times series was located south of the end of the Lomonosov Ridge. This site is ~60 km south of the "ridge" boundary current cross section presented by Lenn et al. (2009), who found that double-diffusive convection dominated vertical fluxes in the upper thermocline. To facilitate measurements, a small opening in the ice was created by vessel maneuvers upon arrival on station.

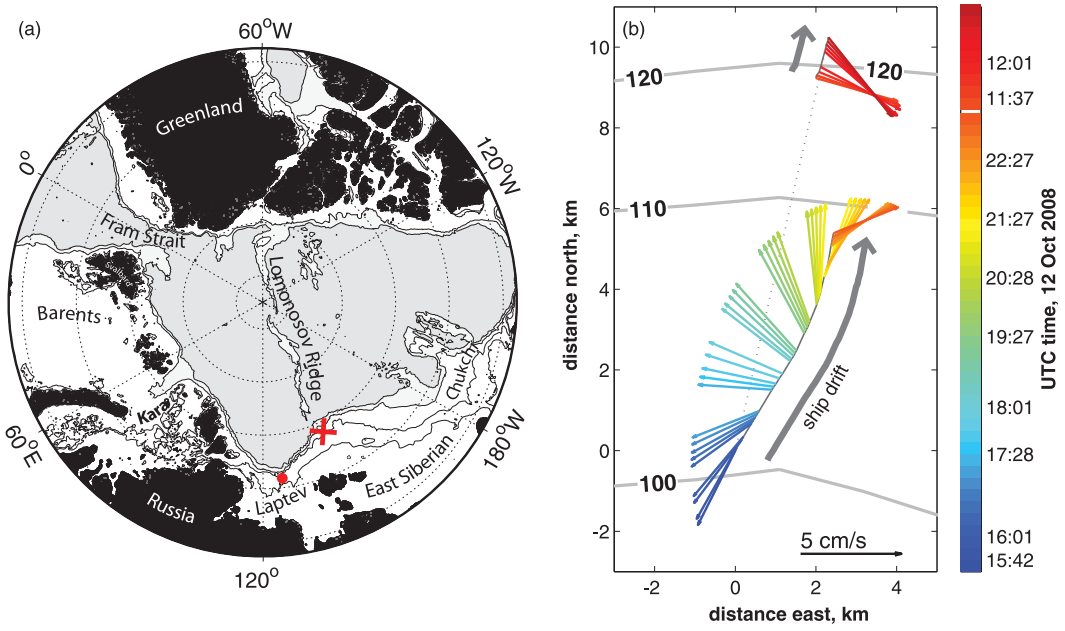

FIG. 1. (a) Map of the Arctic Ocean, marked with the locations of the NLS station (red cross) and the CLS mooring (red dot). (b) NLS time-series station locations relative to 79°12.62′N, 144°51.48′E, with the AOTIM5 tidal currents overlaid on top of bathymetric contours. The path of the station drift is indicated by the thick gray line, and the ship's track during repositioning is indicated by the dotted line. Different colors correspond to the time stamps indicated in the color bar.

This opening (~20-m diameter) was kept free of ice by an outward-directed subsurface sheet of bubbles produced from the ship's portside air bubbler, with the ship resting directly against the ice sheet on the starboard side. Microstructure profiles of shear, temperature (T), and conductivity were collected using a Vertical Microstructure Profiler (VMP), manufactured by Rockland Scientific Instruments and equipped with a 64-kHz Seabird unpumped conductivity–temperature—depth (CTD) instrument (an SBE-3 thermistor and an SBE-4 conductivity cell), deployed through the opening. Between 1100 and 2300 UTC, the ship was allowed to drift freely with the ice sheet while we collected 4–5 VMP profiles within the first 30 min of each hour period, except from 1300 to 1530 UTC, when the ship was repositioning to avoid drifting into deeper water (see ship track: Fig. 1b). The NLS data thus constitute a 12-h time series that includes a 2-h disruption.

The VMP was deployed in free-fall mode with typical fall speeds of ~0.6 m s^{-1} until coming to rest on the bottom and was not recovered onto deck except during the repositioning exercise. Temperature and salinity presented in this study come from the VMP's Seabird instrument. Slow flow rates through the Seabird conductivity cell required that the Seabird conductivity data be calibrated to independent CTD measurements, taken once every 4 h by the instrument on the main CTD rosette, and interpolated in time to each profile. Calibrated VMP–Seabird data at 1-m resolution are used for the salinities (S) presented here. Vertical gradients of T, S, and related quantities are calculated over 2-m intervals ($dz = 2$ m) unless stated otherwise throughout the study.

Microstructure shear data were edited to exclude near-surface observations susceptible to ship-wake and bubbler-induced turbulence, postbottom impact data, and anomalous data spikes. Following Rippeth et al. (2003), turbulent kinetic energy (TKE) dissipation was estimated as $\epsilon = 7.5\mu\langle u_z^2\rangle$ W m^{-3}, where $\mu = 1.88 \times 10^{-3}$ J m^{-3} s is the dynamic viscosity of seawater at 0°C and angle brackets denote the integrated subinertial shear spectrum calculated over 2-s intervals (~1.3-m depth). The instrument noise level is $\sim 2 \times 10^{-7}$ W m^{-3}.

Vertical diffusivities in this study are estimated following Osborn (1980), $K_z = \Gamma\epsilon/\rho_o N^2$, where the mixing efficiency Γ is taken to be 0.2; ρ_o (=1026 kg m^{-3}) is the density of seawater; and $N^2 = g\rho_o^{-1}(d\rho/dz)$ is the buoyancy frequency dependent on gravitational acceleration constant g and density ρ_o. In shear-induced turbulent environments such as the shallow Laptev Sea, our K_z estimates based on $\Gamma = 0.2$ should be considered an upper bound. Heat fluxes are calculated as $F_H = -\rho_o c_p K_z(dT/dz)$ W m^{-2}, where $c_p = 3900$ J kg^{-1} K^{-1} is the specific heat of seawater. Salt fluxes are calculated from $F_s = -1000^{-1}\rho_o K_z(dS/dz)$ kg s^{-1} m^{-2}.

b. Central Laptev Sea observations

This study also includes water velocities from a mooring deployed from August 2006 to July 2007 in the CLS, approximately 520 km away from the NLS site, at 76°44′N, 125°55.3′E in 64 m of water (Fig. 1a). The mooring was deployed during the German–Russian TRANSDRIFT XII/BARKALEV experiment, with an upward-looking Teledyne–RDI Workhorse Sentinel 300-kHz acoustic Doppler current profiler (ADCP) tethered 2-m above the sea floor. The ADCP was configured to profile water column currents, averaged within 2-m depth bins, from 10 m above the instrument to 10 m below the surface every 30 min. In this upward-looking configuration, the bottom tracking mode provided drift velocity of the overhead sea ice during the winter months. In the absence of ice, the ADCP frequently loses tracking and returns missing data values or unrealistically high surface velocities.

The moored ADCP velocities confirm that the semidiurnal tides strongly dominate the Laptev Sea barotropic tides (Figs. 2a,b). Tidal constituents of the ADCP velocities were extracted for each day and each depth from a 28-day window centered on that day (Figs. 2a,b) using the t-tide least squares tidal harmonic routines (Pawlowicz et al. 2002). The barotropic component of the observed tidal currents (Fig. 2c) is derived from averaging the sum of all the tidal constituents over all depths. In equations throughout the text, bold symbols indicate vector quantities such as the ADCP velocities and shear.

Sea ice concentrations used in this study are inferred from the brightness temperatures of the Nimbus-7 Scanning Multichannel Microwave Radiometer (SMMR) and the Defense Meteorological Satellite Program (DMSP) Special Sensor Microwave Imager (SSM/I). The gridded product is provided by the National Snow and Ice Data Center on a polar stereographic grid with cell sizes of 25 km × 25 km (Cavalieri et al. 2008). Because the CLS mooring location proved to be almost equidistant from centers of the four nearest grid cells, we have averaged ice concentrations from all grid cells to estimate the sea ice concentration at CLS. Note that we can expect there to be some discrepancy between the ADCP and the satellite sea ice concentrations, as essentially the satellite estimate covers a 50 × 50 km area, whereas the ADCP would return ice-drift velocities from an area at most 60 m in diameter. In this study, we present the monthly-mean data (1 December 2006–30 April 2007), except during the freezing and melting seasons when the daily-mean data are shown.

c. AOTIM5 Arctic tidal model

Barotropic tides for the NLS time series and CLS mooring locations were derived from Arctic Ocean Tidal Inverse Model (AOTIM5) output (Padman and Erofeeva 2004). This pan-Arctic assimilation model is highly resolved (5-km grid), assimilating data from coastal and benthic tide gauges (between 250 and 310 gauges per tidal constituent) and available satellite altimeters [364 cycles of Ocean Topography Experiment (TOPEX)/Poseidon and 108 cycles of European Remote Sensing Satellite (ERS) altimeter data] to simulate the four most energetic tides: M_2, S_2, O_1, and K_1. Model bathymetry is based on the International Bathymetric Chart of the Arctic Ocean (Jakobsson et al. 2000), and sea ice is not included in the model. AOTIM5 model predictions show the tide propagating across the shelf from CLS to NLS without crossing any amphidromic points; the phase lag between the total CLS and total NLS tide is ~30°. At both NLS and CLS, the tidal currents rotate anticyclonically (clockwise) in time.

Two corrections have been applied to the AOTIM5 predictions presented in this study. First, at the CLS location the actual water depth of 64 m differs from the 68.06 m of the model bathymetry. At the NLS location the difference between the model bathymetry and actual water depth are likewise small, less than 10 m or 9% water depth. The AOTIM5 barotropic tidal predictions have been multiplied by the ratio of model-to-true water depth at each location. Second, Kowalik and Proshutinsky (1994) pointed out that Arctic tides are sensitive to the presence of ice cover, resulting in up to 10% amplitude and 1–2-h phase changes on seasonal time scales. The observed (depth averaged) and model tides at the CLS mooring location during ice-free early September 2006 differed slightly in amplitude but were nearly identical in phase (not shown). By late November, the AOTIM5 tidal currents have slightly smaller amplitudes and lag the observations by about one and a half hours (Fig. 2c). Consequently, given the phase correction implied by the CLS ADCP currents, we advanced all the AOTIM5 predictions for the NLS location by 1.5 h. This phase correction applies to all the figures in which AOTIM5 currents are shown, except Fig. 2.

Both the AOTIM5 and CLS currents show there is a strong spring–neap cycle in the Laptev Sea continental shelf tides, with the deeper NLS currents having smaller amplitudes and a less pronounced spring–neap cycle than at CLS (Fig. 3). The October 2008 NLS observations took place between the neap and spring tides (Fig. 3b). Note that the CLS period shown in Fig. 2 also occurs between the neap and spring tides (Fig. 3a).

d. NLS hydrography

At the NLS time-series location, the water column was stratified with the cold fresh PML ($T < -1.7$°C: Figs. 4a, 5a; $S < 31.5$: Figs. 4b, 5b) separated from warmer and saltier water below by a shallow pycnocline (~20-m

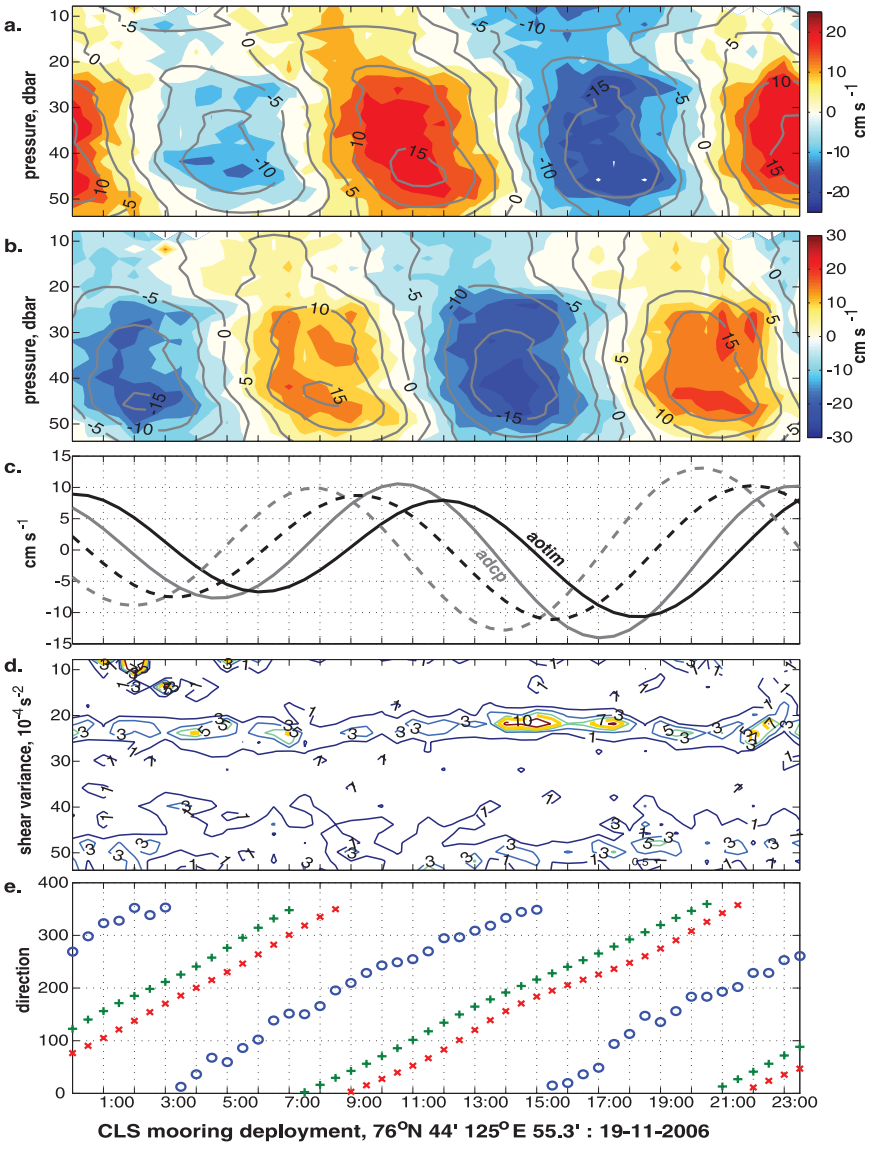

FIG. 2. Time series of CLS data for the 19 Nov 2006 (a) zonal and (b) meridional components of the ADCP currents (color contoured) and the sum of the tidal harmonics (gray contours) are shown. (c) The zonal (solid lines) and meridional (dashed lines) components of the depth-averaged total tidal current from the *t*-tide fit (gray lines) compared to the AOTIM5 simulated barotropic tidal currents (black lines); (d) shear variance $\{(\frac{1}{2})[(\partial u/\partial z)^2 + (\partial v/\partial z)^2]\}$; and (e) the direction of the bulk-shear vector (blue circles), the depth-averaged tidal harmonic sum (green crosses), and the AOTIM5 tidal current (red crosses) are shown.

depth, $-1.7°C < T < -1.5°C$, and $31.25 < S < 32.5$). The NLS pycnocline and water below it were characteristic of the Arctic halocline that is found throughout the Arctic Ocean and marginal seas, and is fresher and cooler than Atlantic- or Pacific-source water (typically $T > 0°C$, $S > 34.5$). During the NLS time series, no dramatic evolution in the stratification was observed (Fig. 4). The slight decrease in water temperature observed below the pycnocline in the first 2 h of observations (Fig. 5a) is more likely due to spatial variability as we drifted off slope over deeper water. A comparison of the potential temperature–salinity (θ–S) curves for the NLS profiles shows a clear divergence in water mass properties below the base of the pycnocline ($S = 32.5$) at the deepest stations (between 1200 and 1400 UTC; Fig. 6).

Stratification favorable to double-diffusive convections typically has density ratios $R_\rho = (\beta\partial S/\partial z)(\alpha\partial\theta/\partial z)^{-1}$, where α and β are the thermal and haline expansion

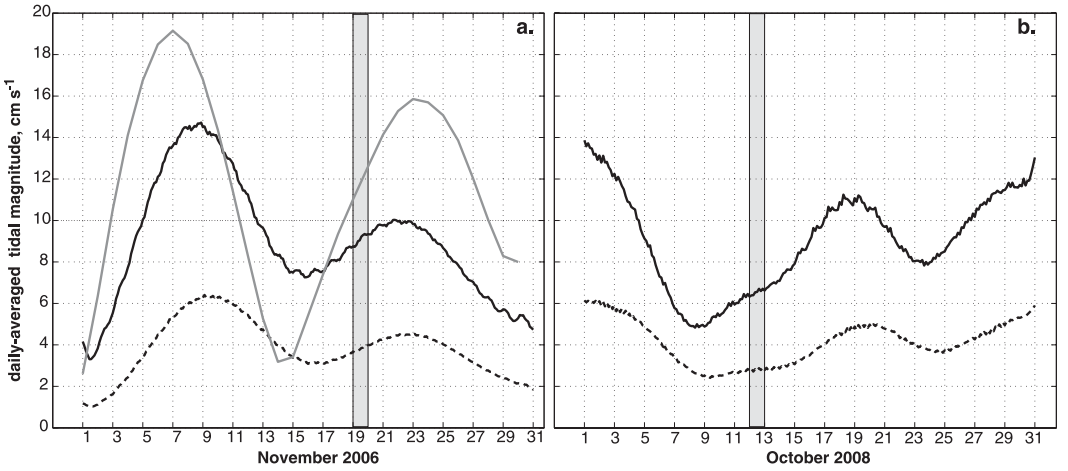

FIG. 3. Daily averaged current magnitude from (a) November 2006 and (b) October 2008. AOTIM5 predictions for CLS (black lines) and NLS (dashed black lines) are shown. The daily averaged and depth-averaged total *t*-tide fit to the CLS ADCP currents (gray line) is shown for November 2006. The NLS observation period (12 Oct 2008) and the period corresponding to CLS currents shown in Fig. 2 (19 Nov 2006) are highlighted by the gray shading.

constants, respectively, greater than one and less than 10 (Kelley et al. 2003). With NLS stratification resulting in R_ρ of $O(10)$, calculated over 5-m depth intervals, there was scant evidence of the telltale thermohaline staircases characteristic of double diffusion. This suggests that, in this continental shelf sea, the expected staircases are eroded by turbulence in contrast to the well-defined upper-thermocline staircases below 100-m depth with $1 \leq R_\rho \leq 3$ observed slightly north over the continental slope (Lenn et al. 2009).

3. Boundary layer dissipation in the NLS

Sea ice can affect Arctic PML dynamics by enhancing the under-ice dissipation beyond levels expected in open water (e.g., McPhee 1992; McPhee and Martinson 1994; McPhee et al. 2003; Fer and Sundfjord 2007), resulting in high vertical heat fluxes that are important for the oceanic ice-mass balance (Maykut and Untersteiner 1971). The NLS observations resolve only a small deep portion of the PML (Figs. 5a–c). This is because NLS profiles were edited to exclude the initial non-free-fall portion of each cast (typically the top 15 m) and spurious turbulence from the air bubbler. Nonetheless, we can say that turbulent dissipation in the PML (above ~20-m depth) is elevated relative to dissipations below the pycnocline and above the bottom boundary layer throughout the time series (Fig. 5a). The PML dissipations ($1–7 \times 10^{-4}$ W m^{-3}) are at least an order of magnitude lower than mixed layer dissipations reported by Sundfjord et al. (2007) and Sirevaag and Fer (2009), from observations in the marginal ice zone of the Barents Sea and on Norwegian Bank just north of Svalbard, respectively.

In continental shelf seas, near-seabed velocities ($\mathbf{U}_b$) produce seabed stresses that in turn drive ϵ and mixing within a bottom boundary layer (BBL). Fluctuating tidal currents ($\mathbf{U}_t$) can interact with ambient residual mean current ($\overline{\mathbf{U}}$) to modulate the near-seabed velocities and stresses, producing an evolving BBL that varies with the tide in a manner most pronounced when the tides are rectilinear (Simpson et al. 1996). The NLS observations were collected during a short drift over 10 km of a gently sloping seabed where phase differences in the AOTIM5 predictions are negligible while the amplitude differences are less than 1 cm s^{-1} and $\overline{\mathbf{U}}$ is unknown. There were also no obvious near-bottom stratification changes under the NLS drift track (Figs. 4, 5) that might affect the tidal profiles and so spatially modify tidal forcing of the BBL mixing. Hence, variability in the BBL ϵ is likely to be due to temporal variability in $\mathbf{U}_t$ or spatial variability in $\overline{\mathbf{U}}$. The NLS seabed TKE ϵ ($\epsilon \sim 10^{-4}$ W m^{-3}) is significantly enhanced over background levels ($\epsilon \sim 10^{-6}$ W m^{-3}) before 1800 UTC (Fig. 5a). Stratification near the seabed in the NLS is weak (Fig. 4d), leading to high vertical diffusivities (K_z; Fig. 5b). This implies a tendency to enhanced vertical mixing of scalars in a bottom boundary layer that extends up to 10 m above the bottom (Fig. 5b).

A comparison of BBL ϵ with the AOTIM5 tidal currents shows that ϵ is clearly enhanced during on-slope tidal flow and weaker when the tidal flow is directed off slope (Figs. 5, 7a). Given the slight local curvature of the continental shelf contours, we have approximated the average on-slope direction as southward and the along-slope direction as eastward. It is possible to estimate the evolution of the shelf currents driving the BBL ϵ if, following Simpson et al. (1996), we assume that, to first order,

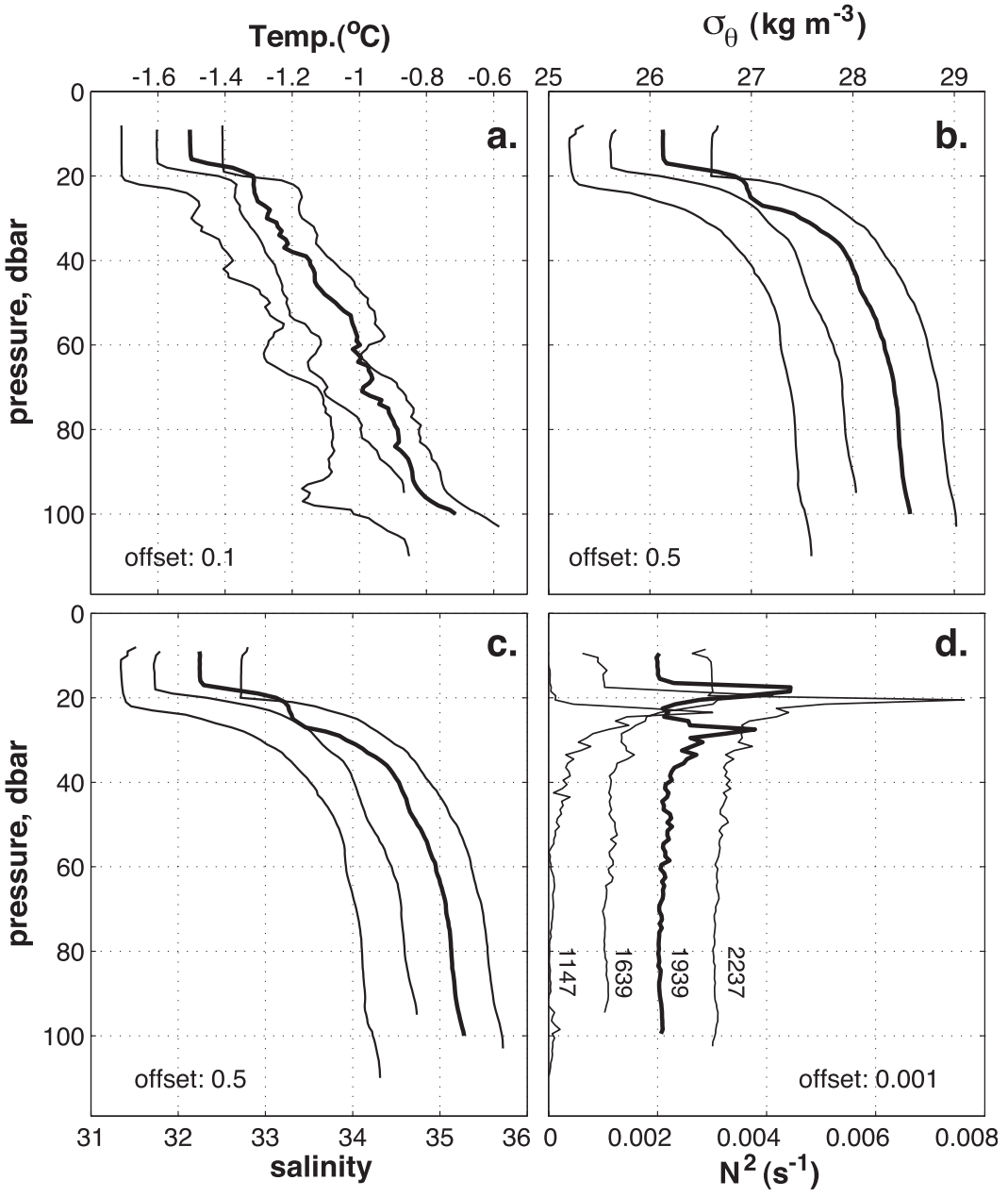

FIG. 4. Hourly averaged NLS profiles of (a) temperature, (b) density ρ, (c) salinity, and (d) buoyancy frequency squared N^2 for 1147, 1639, 1939, and 2237 UTC (see Fig. 5). For clarity, after 1147 UTC, subsequent profiles are each offset from the previous profile by (a) 0.1°C, (b) 0.5 kg m^{-3}, (c) 0.5, and (d) 0.001 s^{-2}. Note that the thick black profile in (a)–(d) occurred during the intense pycnocline mixing event at 1939 UTC.

$$\int_{\mathrm{BBL}} \epsilon \, dz = C_d \rho \mathbf{U}_b |\mathbf{U}_b|^2, \qquad (1)$$

where C_d is the sea bed drag coefficient taken to be 2.5×10^{-3} and $|\mathbf{U}_b| = |\mathbf{U}_t + \overline{\mathbf{U}}|$ is the depth-mean speed. Similarities between $|\overline{\mathbf{U}}|$ estimates and the modeled $|\mathbf{U}_t|$ prior to 1800 UTC (Fig. 5d) suggest that $|\mathbf{U}_t|$ is the primary contributor to near-seabed NLS currents but cannot fully account for the BBL evolution after 1800 UTC (Fig. 5d). Hence, the $|\overline{\mathbf{U}}|$ estimates and the modeled $|\mathbf{U}_t|$ together imply the presence of a small residual $\overline{\mathbf{U}}$. Indeed, a residual mean of $\overline{\mathbf{U}} = \sim 2.3$ cm s^{-1} directed south-southeast (i.e., 72°) over the NLS drift track, in addition to modeled $\mathbf{U}_t$, approximates the magnitude and phase of the $|\overline{\mathbf{U}}|$ estimates (Fig. 5d).

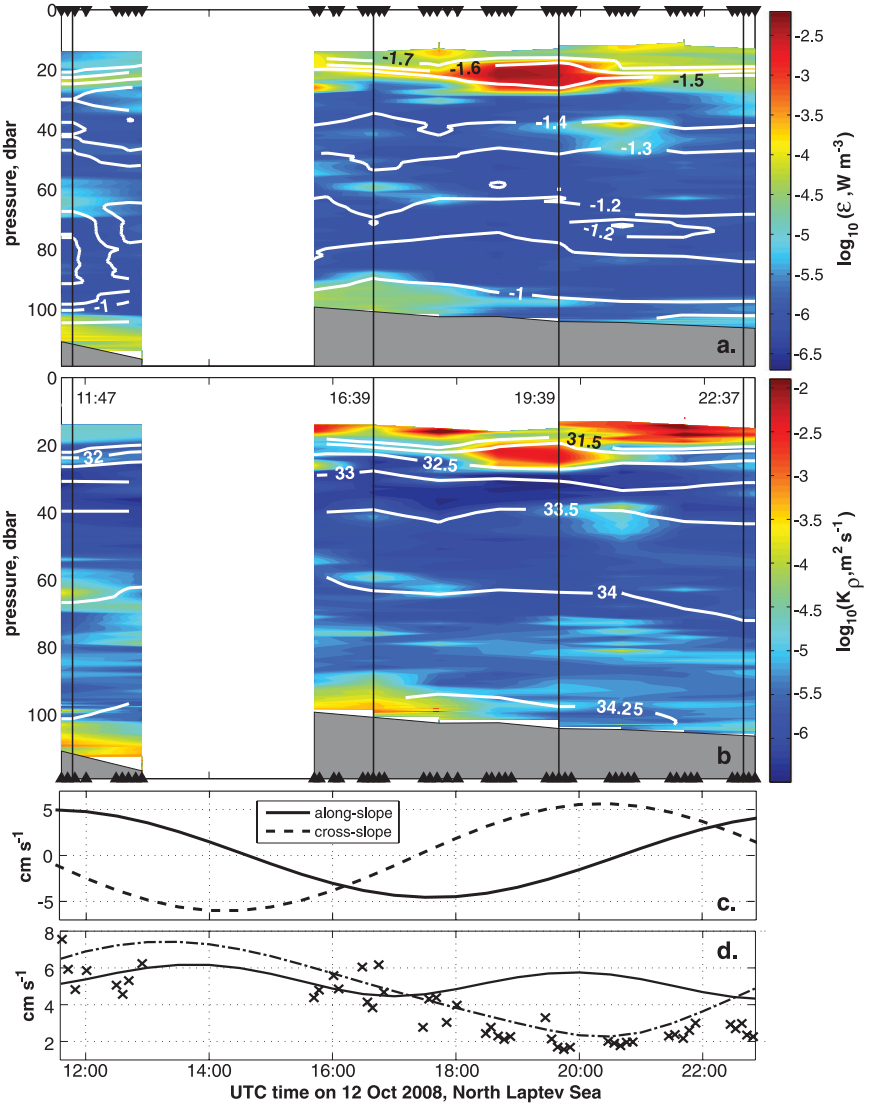

FIG. 5. Time series of (a) contoured TKE dissipation rate $\{\log_{10}[\epsilon(t, z)]\}$, with overlaid contours of temperature (white lines); (b) contoured eddy diffusivity $[\log_{10}(K_z(t, z))]$ with overlaid contours of salinity (white lines); (c) along- and cross-slope components of AOTIM5 tidal currents; and (d) current speed inferred from $\int_{\mathrm{BBL}} \epsilon\, dz = C_D \rho \mathbf{U}_b |\mathbf{U}_b|^2$ (crosses), the AOTIM5 tidal model (solid line), and AOTIM5 plus $\overline{\mathbf{U}}$ (dashed–dotted line). In (a),(b) the microstructure profile times are marked by black triangles, and vertical black lines indicate the average time of the hourly averaged temperature and salinity profiles shown in Fig. 4.

Although speculative, an ambient mean on-slope current of the third the magnitude of the maximum tidal current is consistent with the observed BBL ϵ evolution and would imply the encroachment of continental slope water onto the Laptev Sea continental shelf, where it can be subject to BBL mixing. Modification of bottom boundary mixing arising from an interaction between a residual cross-slope current and the fluctuating tidal flow has been observed elsewhere; in the Ross Sea this has consequences for properties of the shelf water exported to the deep ocean (Padman et al. 2009). Finally, we also note that, because the NLS observations were made slightly closer to neaps than springs (Fig. 3b), our results may be representative of the longer-term average BBL ϵ here.

4. Intermittent enhancement of midwater TKE dissipation and shear

a. *Intermittent NLS pycnocline TKE dissipation*

The most striking feature of the NLS ϵ time series is the patch of very high ϵ ($\sim 10^{-3}$ W m^{-3}) centered at 20-m

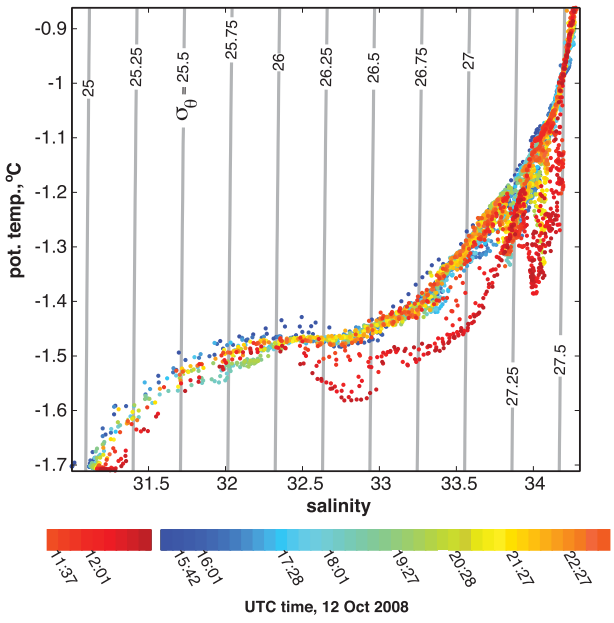

FIG. 6. NLS potential temperature–salinity diagram with the potential density isopycnals relative to the surface (σ_θ) drawn in gray. Different colors correspond to the time stamps indicated in the color bar below.

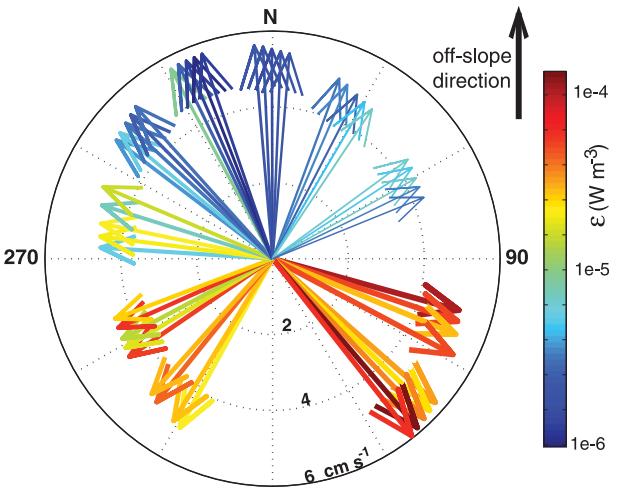

FIG. 7. (a) Compass plot of the AOTIM5 currents predicted for the NLS time series. Arrow colors correspond to ϵ (W m^{-3}) averaged over the 10-m bottom boundary layer; the color scale is shown on the right. Tidal currents rotate clockwise such that the arrow width decreases with time.

depth over a two-hour period between 1800 to 2030 UTC (10 VMP profiles; Fig. 8b). The high ϵ results in enhanced diffusivities ($K_z \sim 5 \times 10^{-4}$ m^2 s^{-1}; Fig. 8b) that are already elevated in the pycnocline ($\epsilon \sim 10^{-4}$ W m^{-3}; $K_z \sim 1.5 \times 10^{-5}$ m^2 s^{-1}) by more than an order of magnitude above background values throughout the time series (Figs. 5a,b). This high ϵ event reduces stratification within the pycnocline (Fig. 4d), resulting in a thickening of the pycnocline, which can be quantified by the separation of the 31.5 and 32.5 isohalines (Figs. 5b, 8a). When the turbulent mixing event concludes, the *TS* step across the pycnocline is rapidly eroded from the top by surface boundary layer mixing.

These observations show that the mixing at the top of the Arctic halocline can be intense but episodic on the Arctic shelves, raising questions about the nature of this intermittency. In the absence of a buoyancy flux and vertical transport of TKE within a fluid, shear instabilities give rise to shear production of TKE that is balanced by viscous dissipation. Hence, the intermittent nature of the intense NLS ϵ event points to an intermittent generation of pycnocline shear. Shear will be concentrated across regions of strong stable stratification such as the NLS pycnocline, which inhibit the vertical transfer of momentum.

In open water, high wind stresses from storms generate large inertial currents that impose high shear across the pycnocline. However, the NLS observations were collected in 100% ice cover, where the only direct air–sea interface was the small patch of water kept open by the ship's air bubbler. We are confident that the ship drift, angle of the VMP wire relative to vertical, and instrument fall speed conspired to place the observations under the ice. Deformation of the ice cover can result in direct transmission of local wind forcing to the underlying ocean (McPhee et al. 2005), but no deformations were observed during the NLS time series. Hence, during the NLS observations, surface stresses exerted on the water were due to the drag of the drifting ice sheet that integrated the effect of local wind stresses over its full areal extent.

NLS ice-drift velocities over ground (Fig. 8), inferred from the ship drift, can be separated into time-averaged ($\overline{\mathbf{V}_{\text{ice}}}$) and transient [$\mathbf{V}_{\text{ice}}(t)$] components. The time-averaged drift speed is 23.04 cm s^{-1} (Fig. 8d) and is directed north-northeast (23.7°; Fig. 8e). The transient component of the drift speed is similar to the predicted tidal speed, varying from 1 to 7 cm s^{-1} (Fig. 8c). The transient component of the drift direction rotates clockwise at a frequency close to semidiurnal, with a large phase lag relative to the predicted tidal currents (Fig. 8e). This rotation rate is suggestive that there is a small near-inertial component present in the ice drift during the NLS observations that may be the result of underlying near-inertial oscillations. Note that the transient drift speed is at a minimum during the high ϵ event (Fig. 8c), and thus high shear required to drive the high ϵ event is unlikely to be due to large-amplitude near-inertial oscillations. It is clear that the magnitude and direction of the drifting ice, and hence the under-ice stress, is dominated by the larger time-averaged component (Fig. 8).

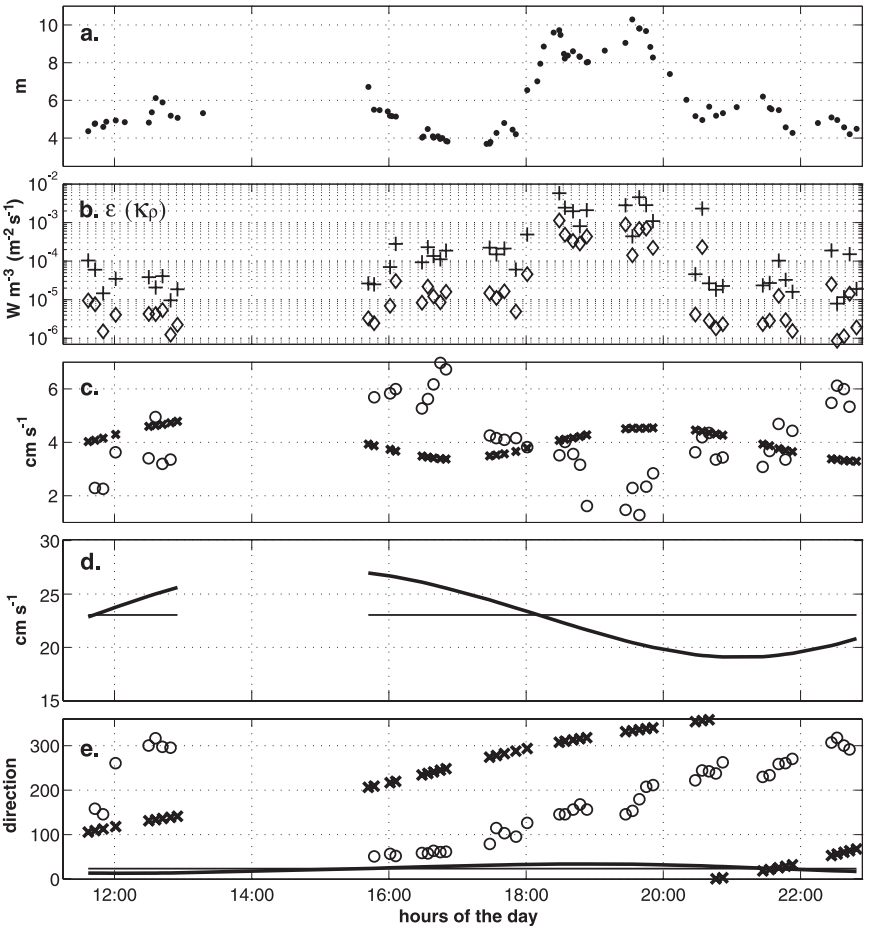

FIG. 8. Time series of (a) the vertical separation of the 31.5 and 32.5 isohalines as a proxy for the pycnocline thickness; (b) layer-mean pycnocline ϵ (pluses) and K_z (diamonds), (c) transient component of the drift speed (circles) and AOTIM5 tidal speed (crisscrosses), (d) the time-mean drift speed ($|\overline{\mathbf{V}_{\text{ice}}}|$; thin line) and relative ice speed ($\mathbf{V}'_{\text{ice}}|$ thick line), and (e) time-mean drift direction (thin line), relative ice-drift direction (thick line), transient drift direction (circles), and AOTIM5 barotropic tide direction (crisscrosses).

Under-ice stresses are typically calculated using a quadratic drag law in which the drag coefficient depends on the roughness of the underside of the ice, and the velocity is taken to be the ice-water relative velocity rather than the free drift ice velocity (McPhee 2002, and references therein). Assuming that the transient component of the drift results from underlying near-inertial currents, then the ice-water relative velocity can be estimated from the difference between the time-averaged component of the ice drift and the predicted barotropic tide ($\mathbf{V}'_{\text{ice}} = \overline{\mathbf{V}_{\text{ice}}} - \mathbf{V}_{\text{tide}}$). Consequently, the surface stress will fluctuate predominantly with the rotating tidal currents (Fig. 1b), achieving a maximum once every tidal cycle when relative ice-water velocity is maximum (Fig. 8d). The NLS $|\mathbf{V}'_{\text{ice}}|$, and consequently surface stress, was maximum shortly before 1600 UTC (Fig. 8d), approximately 4 h before the intense ϵ event. Clearly, the large impulse in under-ice stress from localized wind forcing or other sources required to drive the dramatic peak in ϵ is conspicuously absent from the record.

b. Variability in pycnocline shear at CLS

The CLS ADCP velocities provide some insight on the nature of the baroclinic currents and associated pycnocline shear that may be present at the NLS site. Pronounced vertical shear in the tidally dominated horizontal ADCP currents is clearly present 20–25 m from the surface, such that the currents above 24-m depth lead the underlying currents (Figs. 2a,b). CTD observations in close proximity to this site, made during the NABOS/ASBO September 2007 expedition, confirm that this corresponds to the depth of the pycnocline (Abrahamsen et al. 2008) in what is essentially a two-layer system. To characterize the pycnocline shear, we computed the bulk-shear

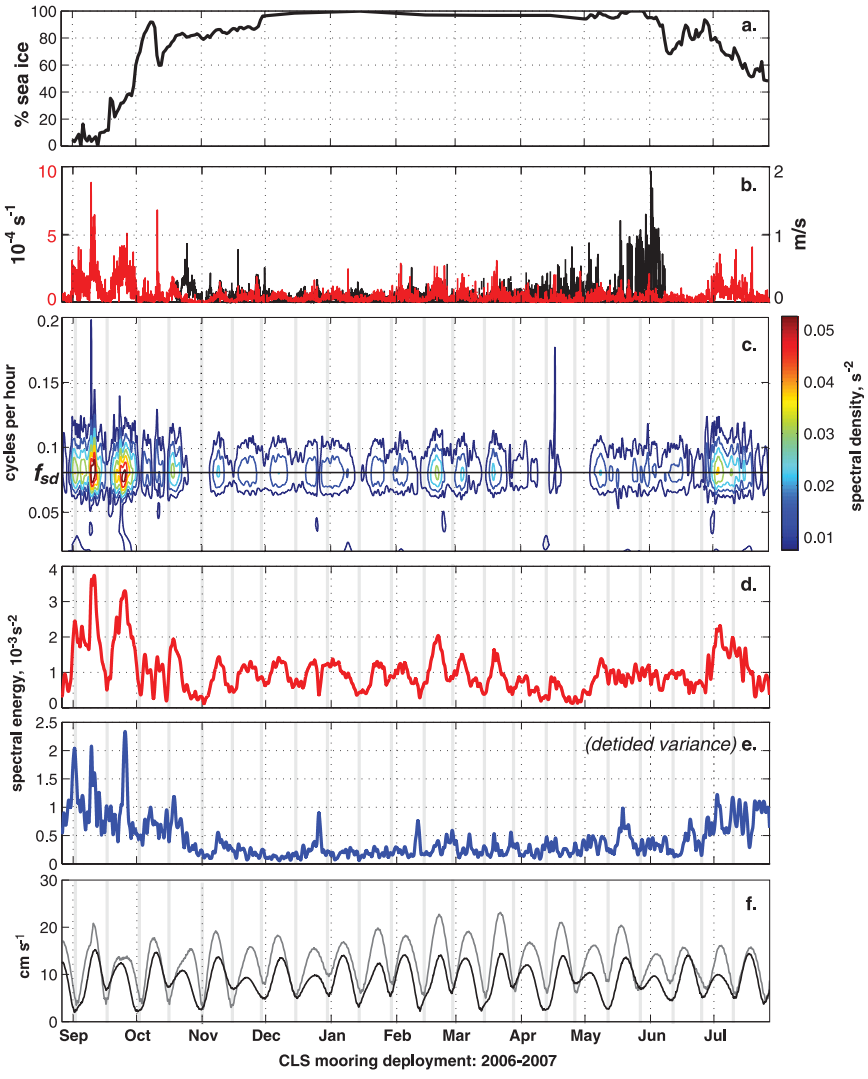

FIG. 9. CLS time series of (a) Nimbus-7 SMMR and DMSP–SSM/I sea ice concentrations; (b) bulk-shear squared amplitude S_b^2 (red line; scale at left) and relative surface velocity amplitude $|\mathbf{V}'_{\text{ice}}|$ (black line; scale at right); (c) $\hat{S}_b$ spectral density of the wavelet spectra for the zonal bulk-shear component; f_{sd} band-integrated variance of the (d) zonal wavelet spectra ($\langle \hat{S}_b \rangle_{f_{\text{sd}}}$; red line) and (e) detided zonal wavelet spectra (blue line); (f) magnitude of the depth-averaged ADCP currents (gray line) and AOTIM5 tidal currents (black line). The occurrences of the neap tides are indicated by the thick light gray lines in (c)–(f).

vector $\mathbf{S}_b$ by differencing the top (10–14-m depth) and bottom (30–44-m depth) layer-averaged ADCP currents and dividing by the mean separation of the layers (25 m). The relative ice velocity is calculated by subtracting the depth-averaged velocity of the two uppermost ADCP bins from the ice-drift velocity, given by the "bottom tracking" returns of the upward-looking ADCP, $\mathbf{V}'_{\text{ice}} = \mathbf{V}_{\text{ice}} - \mathbf{V}_{\text{water}}$.

Rotary spectral analysis of the CLS time series provides an assessment of the $\mathbf{S}_b$ variability and rotational polarization on seasonal and shorter time scales. To assess seasonal differences in the bulk shear, we have computed the rotary spectra for the ice-covered winter (mid-October 2006 to late May 2007) and relatively ice-free summer (all other times). Note that satellite observations show that sea ice at CLS advanced rapidly from near zero to 80% concentration over a month-long period beginning in mid-September 2006, achieving 100% concentration in late November 2006 (Fig. 9a). However, the CLS ADCP ice-drift data transitioned from noisy intermittent returns to values consistent with the continuous presence of drifting overhead sea ice in late October 2006 (Fig. 9a). Hence, we believe that the CLS ice pack became consolidated somewhat earlier than the satellites imply and have

chosen to delineate the ice-covered season accordingly. Because the observations were close to the M_2 critical latitude, the rotary spectra do not separate out the semidiurnal tides and inertial frequencies for this time series, because both are anticyclonically polarized (+ and − superscripts henceforth indicate anticyclonic and cyclonic polarization, respectively). From here on, we refer to a semidiurnal frequency band f_{sd} centered at 0.0810 cph with half-peak bandwidth of 0.0062 cph that includes the principal semidiurnal lunar M_2 (0.0806 cph) and solar S_2 (0.0833 cph) tidal harmonics and f (0.0815 cph).

Area-preserving $\boldsymbol{S}_b^+$ spectra are strongly peaked over the f_{sd} frequency band in both seasons (Fig. 10a) and contain virtually no energy at other frequencies in either season. Clearly, the anticyclonic summer f_{sd} peak possesses more than twice the energy of the winter f_{sd} peak (Fig. 10a), a seasonal difference that is statistically significant at 95% confidence. In comparison, the $\boldsymbol{S}_b^-$ spectra contain no energy at any frequency resolved (Fig. 10a). Rotary spectra presented on log–log axes highlight other differences between the polarizations and seasons. At frequencies below f_{sd}, there is no statistically significant polarization of the summer $\mathbf{S}_b$ spectrum (Fig. 10b). Conversely, in winter, at frequencies greater than 0.01 cph, we can say with 95% confidence that the anticyclonic $\mathbf{S}_b^+$ spectrum is greater than $\mathbf{S}_b^-$ spectrum and peaks at the P_1/K_1 diurnal frequencies (Fig. 10). There is also a statistically significant difference in the width of the summer and winter f_{sd} peaks (Fig. 10b). The winter f_{sd}^+ peak is much narrower at its base than the summer f_{sd}^+ peak, which contains energy spread over a wider semidiurnal frequency range from 0.06 to 0.11 cph (Fig. 10b).

Wavelet spectral analysis (Liu 1994) allows us to better resolve how $\mathbf{S}_b$ variability evolves with time. The Morlet wavelet spectra (indicated by ˆ) for the zonal and meridional $\hat{S}_b$ components are very similar because of the rotary nature of the shear, thus for clarity we present only the full spectral results for the zonal component (Fig. 9c). As in the rotary spectra, the variance is concentrated in the f_{sd} band (Fig. 9c). By integrating the zonal and meridional wavelet spectra across the f_{sd} band, we can focus on the evolution of the semidiurnal variability in $\hat{S}_b$ (Fig. 9c). The wavelet analysis was also repeated for "detided" ADCP velocity shear, from which the total tides fit as described in section 2b have been subtracted. The detided wavelet spectrum was also strongly peaked in the f_{sd} band (not shown), and the variance contained within this peak can be mainly attributed to inertial current shear ($\hat{S}_i$; Fig. 9e).

The wavelet spectra analysis clearly demonstrates that tidal forcing is an important component of the variability in the CLS currents in all seasons, particularly in winter. Subtracting the tidal harmonics reduced the variance contained in $\hat{S}_i$ relative to $\hat{S}_b$ by ~30% in summer and ~75% in winter (note different scales in Figs. 9d,e). The beating of the M_2 and S_2 tidal harmonics results in a spring–neap tidal cycle that is also apparent in $\hat{S}_b(f_{sd})$ (Fig. 9d). This spring–neap tidal modulation is clearest from late October 2006 to mid-April 2007 under near-100% ice cover and diminishes with the loss sea ice due to the increased presence of randomly phased inertial currents (Fig. 9d).

The wavelet spectra also clearly show that the large decrease in f_{sd} variance (Figs. 9c,d) seen in late October

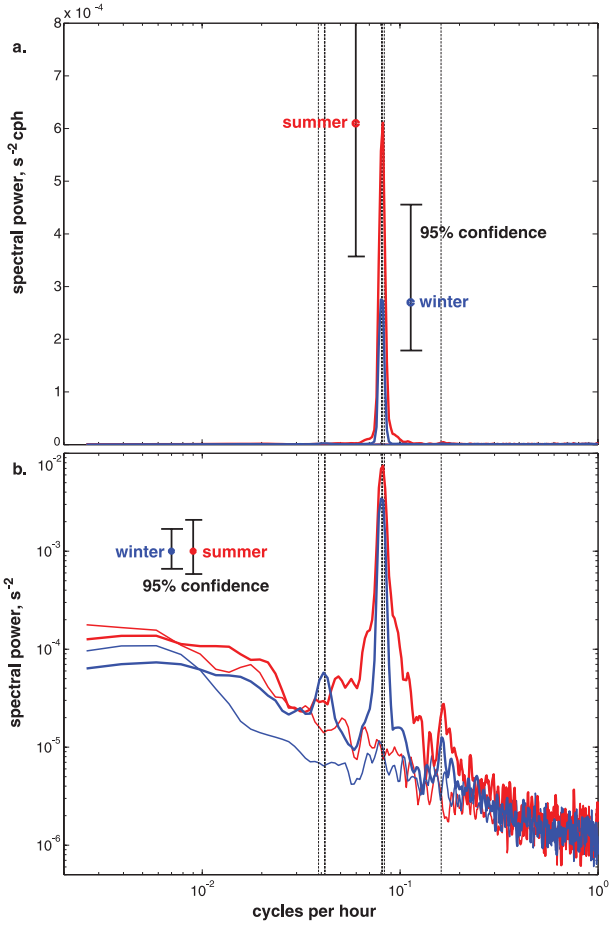

FIG. 10. Rotary spectra plotted in (a) area-preserving form and (b) against a log–log axis of $\mathbf{S}_b$ for the winter (blue lines: mid-October 2006 to late May 2007) and summer (red lines: all other times). Anticyclonic (clockwise rotating) and cyclonic (anticlockwise rotating) components are plotted as thick and thin lines, respectively. Dotted lines indicate frequencies of the principal diurnal tides O_1, P_1, and K_1 (0.0387–0.0418 cph); the dominant semidiurnal tide M_2 (0.0806 cph); inertial f (0.0815 cph); S_2 (0.0833 cph); and the quarter-diurnal tide M_4 (0.1613 cph). Note that the lines corresponding to the M_2 and inertial frequencies are so close as to be not clearly distinct at this scale: likewise for the P_1 and K_1 lines. Note that the 95% confidence intervals in (a) apply to the semidiurnal peak values of each spectrum, whereas in (b) they apply over the all the frequencies resolved.

2006 is consistent with attenuation of wind momentum transferred to surface-intensified near-inertial currents ($\hat{S}_i$; Fig. 9e) by the advancing sea ice (Fig. 9a). The f_{sd} variance remains low until late May 2007, when the sea ice retreats. Our wavelet and rotary spectral analyses show that the CLS currents are highly sensitive to the presence of sea ice, such that there is a striking increase in pycnocline shear due to wind-forced near-inertial currents in the absence of sea ice. These results are also in strong agreement with the observations made by Rainville and Woodgate (2009) in the marginal Chukchi Sea of the western Arctic. Taken together, the Laptev and Chukchi Sea observations provide clear evidence that there is considerably more kinetic energy available to drive vertical mixing in the Arctic continental shelf seas during ice-free periods than during periods of ice cover. In a changing Arctic, where sea ice concentrations are reduced, this suggests that the Arctic continental shelves will become ever more energetic mixing environments.

5. Discussion

a. Episodic generation of midwater mixing

In the Arctic marginal seas, the tides are also subject to critical latitude effects (i.e., where the local inertial frequency f matches the semidiurnal tidal frequencies: e.g., 74°28′18″N and 85°45′54″N for M_2 and S_2, respectively). Close to or at the critical latitudes for given tidal constituents, these constituents become strongly depth dependant (e.g., Prinsenberg and Bennett 1989; Furevik and Foldvik 1996) and sensitive to stratification (e.g., Makinson 2002). Models and observations show that the rotational polarization of the tide, together with the stratification, are determining factors in boundary layer thickness (e.g., Simpson and Tinker 2009), effects that becomes acute at critical latitudes (Prandle 1982; Furevik and Foldvik 1996; Makinson et al. 2006; Daae et al. 2009). The near-critical anticyclonic tidal component generates significantly thicker bottom boundary layers that can extend high up into a weakly stratified water column, resulting in higher mixing over a greater depth range than the cyclonic component. Both the CLS and NLS sites are located between the M_2 and S_2 critical latitudes, and they are characterized by AOTIM5 barotropic tidal currents that are strongly clockwise polarized (i.e., anticyclonic) and have a large M_2 component. At NLS, relatively weak tidal currents result in a thin BBL, which is unconnected to the high ϵ episode in the pycnocline (Fig. 5a).

Tidal harmonic decomposition of the CLS currents shows that the M_2 tidal ellipses are markedly sheared with a midwater maximum (not shown,) as expected near the critical latitude (Prinsenberg and Bennett 1989; Furevik and Foldvik 1996; Makinson et al. 2006). Observations and models have shown that the midwater maxima in the near-critical M_2 currents (<26 cm s^{-1}) results from a decoupling of the under-ice and bottom boundary layers from the water column around the pycnocline (Prinsenberg and Bennett 1989; Makinson 2002). Given the small tidal currents at CLS, it is unlikely that the surface and bottom boundary layers can grow to sufficient thickness to strongly impact pycnocline shear. Rather, the pycnocline shear at CLS arises from the shear above the midwater M_2 maximum and is separated from the shear below the midwater M_2 maxima that drives CLS BBL ϵ. Consequently, we can expect an increase in $\mathbf{S}_b$ as the semidiurnal M_2 tidal current at CLS approaches its maximum free-stream velocity on quarter-diurnal time scales. However, the $\mathbf{S}_b$ is dominated by semidiurnal, rather than quarter-diurnal, variability in the CLS. Thus, critical latitude effects can account for the baroclinicity of the M_2 tide but do not fully explain variability in $\mathbf{S}_b$.

A closer examination of bulk-shear squared ($S_b^2 = |\mathbf{S}_b|^2$) shows regular enhancement of S_b^2 on semidiurnal time scales (Fig. 11a). This is true throughout the CLS record and not just for the 3–4-day mid-November 2006 period (Fig. 11) chosen for comparison because of similarities with the environmental conditions of the 2008 cruise. During this period, there were no large fluctuations in $\mathbf{V}'_{\text{ice}}$, except early on November 18 (Fig. 11a). The lack of correlation between S_b^2 and changes in amplitude or phase of $\mathbf{V}'_{\text{ice}}$, (Figs. 11a,c), unless these were unusually large and abrupt, discounts the possibility that intermittent generation of near-inertial currents by the under-ice stress is responsible for enhancing the bulk shear. Instead, the under-ice stresses may play a different role in generating the enhanced shear observed.

Rippeth et al. (2009) recently described short episodic bursts of enhanced shear across the temperate continental shelf sea thermocline that were correlated with enhanced ϵ, resulting in intermittent mixing within the thermocline. Solving a simple two-layer one-dimensional model of a stratified tidal shelf sea forced by a surface wind stress, BR09 predicted that the time rate of change in bulk-shear squared S_b^2 is

$$\partial_t S_b^2 = \frac{4}{h}\mathbf{S}_b \cdot \left(\frac{\tau_s}{h_s} + \frac{\tau_l}{h_l}\right) - c_i \frac{h^2}{h_s h_l} S^3, \qquad (2)$$

where h is the sum of the h_s upper- and h_l lower-layer thicknesses, $\boldsymbol{\tau}_s$ and $\boldsymbol{\tau}_l$ are the surface and bed stresses, and c_i is the interfacial form drag coefficient. In other words, S^2 is produced or destroyed by an interaction between $\mathbf{S}_b$ and the sum of the layer-weighted surface and bed stresses, and it is dissipated by interfacial friction. With this model, BR09 were able to accurately predict the bulk-shear

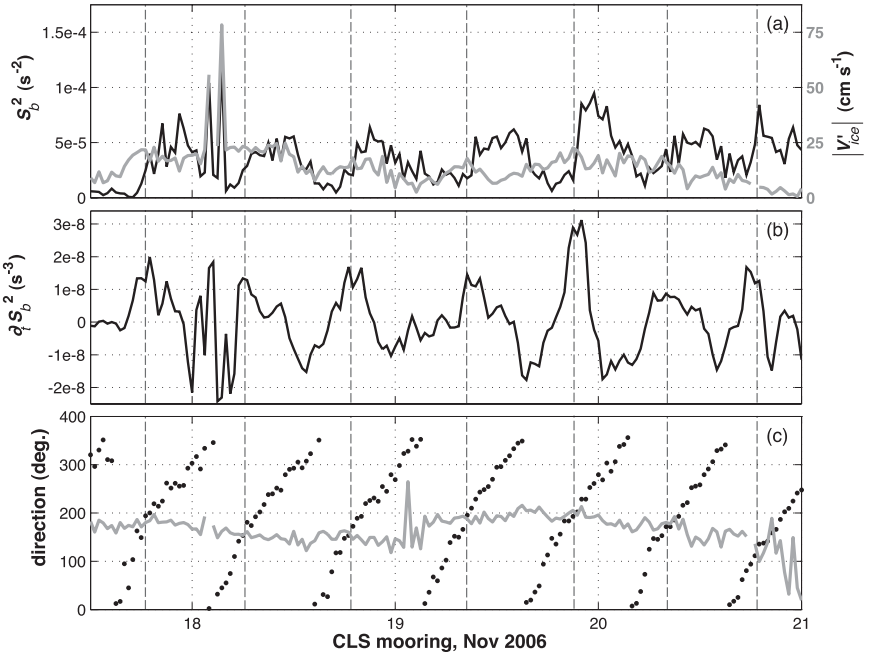

FIG. 11. Time series of CLS data for four days in November 2006: (a) squared amplitude of bulk shear (S_b^2, black line; scale at left) and amplitude of relative ice velocity ($|\mathbf{V}'_{\text{ice}}|$; gray line; scale at right); (b) rate of shear generation ($\partial_t S_b^2$), smoothed by a 2-h moving average; and (c) direction of the bulk shear (black dots) and the direction of the relative ice velocity [gray line; directions are given relative to north (0°)]. The vertical dashed lines indicate the times at which the bulk-shear vector is in alignment with the relative surface velocity.

spiking resulting from an alignment between $\mathbf{S}_b$ and $\boldsymbol{\tau}_s$ (which was $\gg \boldsymbol{\tau}_l h_s h_l^{-1}$) observed during summer stratified conditions in the northern North Sea.

Under early winter ice-covered conditions in the CLS, both the $\mathbf{S}_b$ and $\boldsymbol{\tau}_l$ are strongly dominated by the semidiurnal tides (Fig. 10a). It follows then that the phase difference between $\mathbf{S}_b$ and the bottom tidal currents will be relatively constant barring abrupt and large changes in the stratification. Hence, the bed stress component of the shear generation term in Eq. (2) is unlikely to provide intermittent forcing. Episodic generation of S_b^2 will mainly arise from an alignment between the anticyclonically rotating $\mathbf{S}_b$ and the surface stress term, which depends on $\mathbf{V}'_{\text{ice}}$, To test this hypothesis, we computed $\partial_t S_b^2$ (Fig. 11b) from the measured time rate of change of S_b^2 (Fig. 11a), applying a 2-h running mean to reduce the noise. Each occasion on which the semidiurnally rotating $\mathbf{S}_b$ comes into alignment with the slowly varying $\mathbf{V}'_{\text{ice}}$, direction (Fig. 11c) coincides with a peak in shear generation (Fig. 11b) immediately followed by an enhancement of S_b^2 (Fig. 11a). Thus, the BR09 model is a plausible mechanism for the episodic production of high shear under ice in the Arctic shelf seas, which can remain stratified over large areas even in winter, and may also be important in ice-free conditions when higher shears are observed (Fig. 9a).

According to BR09, S_b^2 remains high until interfacial friction dissipates the shear or is destroyed when $\mathbf{S}_b$ rotates 180° out of phase with $\boldsymbol{\tau}_s$ (Fig. 11c). For the period shown, our results indicate that the S_b^2 is rapidly destroyed when the $\mathbf{S}_b$ rotates into 180° misalignment with $\boldsymbol{\tau}_s$, but asymmetry in many of S_b^2 peaks is evidence of interfacial dissipation eroding the shear. Note that the interfacial frictional dissipation is itself dependent on S_b^2 [Eq. (2)] and hence will be highest just after the $\partial_t S_b^2$ peaks, which last on average 2–3 h (Fig. 11). The $\partial_t S_b^2$ peaks ($>10^{-8}$ s^{-3}) are similar in duration to the episode of enhanced pycnocline ϵ observed in the NLS. The proximity to the M_2 critical latitude and presence of a strong pycnocline implies that at the NLS site, as in the CLS, strongly sheared clockwise-rotating M_2 tidal currents dominate (Fig. 8e). Under these circumstances, the BR09 shear spiking mechanism provides a plausible explanation for the high-ϵ event. Furthermore, if the phase of NLS $\mathbf{S}_b$ is dominated by the M_2 tide instead of randomly phased inertial oscillations, then the timing of the intense mixing episode implies that the pycnocline shear vector leads the barotropic tide by about 4 h in the NLS (see Fig. 8). Concurrent turbulence and velocity observations will be needed to evaluate this process.

b. Impact of dissipation on Laptev Sea heat and salt fluxes

The NLS observations were made slightly less than halfway between the nearest neap and spring tides (Fig. 3b) and as such may be viewed as representative of a near-average state. Upward heat and salt fluxes associated with the NLS BBL peaked at 4–8 W m^{-2} and 0.5–1.5 $\times$ 10^{-6} kg s^{-1} m^{-2}, respectively, during periods of enhanced ϵ. These heat fluxes are smaller than the 15 W m^{-2} near-bottom heat flux that Fer et al. (2010) reported in the West Spitsbergen Current as it flowed close to the continental shelf north of Svalbard. This spatial variability is to be expected, because the tides and internal wave field are known to be much stronger in the vicinity of the Yermak Plateau and Svalbard than the NLS. Nonetheless, the NLS fluxes are considerably higher than the $\leq$1 W m^{-2} upward heat fluxes in the upper thermocline reported by Lenn et al. (2009) only ~60–200 km to the north of the NLS site. Furthermore, the NLS heat fluxes are consistent with observations that show warming of the Laptev Sea bottom water from heat lost from warm AW encroaching onto the continental shelf (see Fig. 12 of Dmitrenko et al. 2010). This suggests that the transformation of Atlantic Water flowing in the boundary current, unexplained by offshore double-diffusive heat fluxes (Lenn et al. 2009), may occur primarily on the edge of the continental shelf seas. Our results highlight the importance of inertial and tidal mixing on the Arctic continental shelves and shelf–basin exchange for Arctic Ocean hydrography predicted by Holloway and Proshutinsky (2007).

Higher up in the water column, diapycnal heat fluxes into the PML from below are ~54 W m^{-2} during the intense ϵ event and ~2 W m^{-2} during the remainder of the observations. This gives an average upward heat flux of ~12 W m^{-2} over the duration of the NLS observation period. These fluxes compare well with observations in the Barents Sea (Fer and Sundfjord 2007) and smaller than the very large [O(300 W m^{-2})] pycnocline heat fluxes reported by Sirevaag and Fer (2009) for the shallow ($\leq$80-m depth) Norwegian Bank region. Differences between NLS and the Norwegian Bank result from a combination of slightly higher K_z (10^{-3}–10^{-2} W m^{-2}) and stronger temperature stratification in the Norwegian Bank region. As earlier studies show (Padman and Dillon 1991; D'Asaro and Morison 1992), pycnocline fluxes over significant topography are considerably higher than fluxes observed over the abyssal Arctic interior basins (Rainville and Winsor 2008; Fer 2009).

NLS pycnocline salt fluxes peak at ~170 $\times$ 10^{-6} kg m^{-2} s^{-1} compared with ~1 $\times$ 10^{-6} kg m m^{-2} s^{-1} at other times, resulting in a time-averaged upward flux of ~30 $\times$ 10^{-6} kg m^{-3}. The NLS pycnocline salt fluxes compare very well with the Norwegian Bank pycnocline salt fluxes (33 $\times$ 10^{-6} kg m^{-3}) reported by Sirevaag and Fer (2009) because, despite weaker K_z, the salinity stratification is stronger across the NLS pycnocline. These upward salt fluxes are associated with a net downward freshwater flux from the PML into the halocline-class shelf waters.

The Arctic heat and salt flux rates discussed here come from short-term studies that do not necessarily resolve the spring–neap cycle, much less the annual cycle. Certainly, one expects spatial variability and temporal variability to affect the comparisons between studies. However, the results of this study clearly demonstrate how intermittent high-ϵ events, although short lived, can dominate water mass transformations on the Arctic shelves. It is this very intermittency in mixing events that makes observing them and achieving good average estimates nontrivial.

6. Conclusions

In this study, we investigate intermittent diapycnal mixing in the Laptev Sea continental shelf, using a rapidly sampled 12-h time series of microstructure temperature, conductivity, and shear observations made during October 2008 in the northern Laptev Sea under 100% ice cover. This was complemented by moored ADCP observations taken in the central Laptev Sea from August 2005 to July 2006.

The rare NLS microstructure dataset, collected over one semidiurnal period, allowed us to resolve the temporal evolution of TKE ϵ under ice (Fig. 5). Enhancement in bottom boundary ϵ ($\epsilon \sim 10^{-4}$ W m^{-3}; Fig. 5a) beyond background levels ($\epsilon \sim 10^{-6}$ W m^{-3}) is observed up to 10 m above the seabed (Fig. 5a) for half of the semidiurnal tidal cycle, in a manner consistent with the interaction of the fluctuating tide with a mean on-slope current (Fig. 7).

The most striking feature in the ϵ time series is an isolated episode of exceptionally high ϵ (Fig. 5a) and vertical diffusivities (Fig. 5b) in the pycnocline that lasted for two hours. This high ϵ event could not be accounted for by any localized wind-forced impulse in the surface stress. Rather, regional CLS observations suggest that baroclinic tides and inertial currents give rise to a rotating pycnocline shear vector that is amplified on semidiurnal time scales following alignment with the under-ice surface stress. These results are consistent with a mechanism proposed by BR09 for the generation of shear spikes that lead to episodic mixing in wind-forced stratified midlatitude shelf seas.

Spectral analysis of the bulk shear in the CLS currents further reveals that the availability of wind-driven inertial shear is greatly enhanced in the absence of sea ice cover (Figs. 9, 10). This implies that the shear spiking mechanism

may drive mixing with much greater frequency and intensity during the Arctic summer months as compared to winter when the semidiurnal tides are the principle contributors to the pycnocline shear.

In summary, we found that both intermittent pycnocline and tidally induced bottom boundary mixing occurs in the Arctic shelf seas. Bottom boundary mixing drives upward peak heat fluxes of ~4–8 W m^{-2} that average out to ~2 W m^{-2} over the tidal cycle in the north Laptev Sea. Consequently, continental shelf bottom boundary mixing can more than double the rate of heat lost from the AW by the primary process of double diffusion in the nearby Arctic boundary current over deep water (Lenn et al. 2009).

The intense mixing event observed in the Laptev Sea pycnocline drove upward heat fluxes of ~54 W m^{-2} when ε was at a maximum (~2 W m^{-2} at other times), resulting in a 12-h average of ~12 W m^{-2} fluxes, which is comparable to Barents Sea observations (Fer and Sundfjord 2007) and much higher than in the interior Arctic Ocean (Rainville and Winsor 2008; Lenn et al. 2009; Fer 2009). This intermittent mixing event dominated the total NLS pycnocline mixing observed over a semidiurnal cycle occurring between the neap and spring tides, resulting in heat lost from and corresponding freshwater influx to the Arctic halocline. In addition to modification of the halocline, the cross-pycnocline heat fluxes provide heat to the PML, which has implications for the oceanic ice-mass balance (e.g., Maykut and Untersteiner 1971; Padman and Dillon 1987; McPhee and Martinson 1994; Fer and Sundfjord 2007).

Our main conclusions are threefold. First, the shear-enhancement mechanism proposed has relevance to the Arctic shelves, and both winds and tides contribute to mixing on the Arctic continental shelf seas. Second, Arctic shelf sea mixing, although intermittent, can impact the modification of Arctic water masses. Third, the availability of inertial current shear to drive mixing in the Arctic shelf seas strongly depends on the absence of sea ice. More investigation is clearly required, not just on specific episodic mixing mechanisms but also on their frequency and distribution under ice and particularly in ice-free conditions, when our observations show higher pycnocline shear conducive to more intense mixing. Future research will be necessary to improve our understanding of the nature of Arctic shelf sea mixing and exchange with the Arctic interior and therefore to improve parameterization of these subgrid-scale processes in the climate models.

Acknowledgments. This microstructure data were collected under the U.K. Natural Environment Research Council ASBO Arctic IPY Consortium Grant, with additional support for the analysis provided by the NERC Grants NE/F002432 and NE/H016007/1. The authors thank their partners at IARC, Fairbanks, and the captain and crew of the I/B *Kapitan Dranitsyn*. We acknowledge Ben Powell for his essential technical support. This study has been much improved by constructive feedback from Laurie Padman and Ilker Fer.

REFERENCES

Aagaard, K., L. Coachman, and E. Carmack, 1981: On the halocline of the Arctic Ocean. *Deep-Sea Res.,* **28A,** 529–545.

Abrahamsen, E. P., and Coauthors, 2008: Tracer-derived freshwater composition of the Siberian Continental Shelf following the extreme Arctic summer of 2007. *Geophys. Res. Lett.,* **36,** L07602, doi:10.1029/2009GL037341.

Burchard, H., and T. P. Rippeth, 2009: Generation of bulk shear spikes in shallow stratified tidal seas. *J. Phys. Oceanogr.,* **39,** 969–985.

Cavalieri, D., C. Parkinson, P. Gloersen, and H. J. Zwally, 2008: Sea-ice concentrations from Nimbus-7 SMMR and DMSP SSM/I passive microwave data [August 2006–July 2007]. National Snow and Ice Data Center, Boulder, CO, digital media. [Available online at ftp://sidads.colorado.edu/pub/DATASETS/seaice/polar-stereo/nasateam/final-gsfc/.]

Daae, K. L., I. Fer, and E. P. Abrahamsen, 2009: Mixing on the continental slope of the southern Weddell Sea. *J. Geophys. Res.,* **114,** C09018, doi:10.1029/2008JC005259.

D'Asaro, E. A., and J. H. Morison, 1992: Internal waves and mixing in the Arctic Ocean. *Deep-Sea Res. I,* **39,** S459–S484.

Dmitrenko, I. A., and Coauthors, 2010: Impact of the Arctic Ocean Atlantic water layer on the Siberian shelf hydrography. *J. Geophys. Res.,* **115,** C08010, doi:10.1029/2009JC006020.

Fer, I., 2009: Weak vertical diffusion allows maintenance of cold halocline in the central Arctic. *Atmos. Oceanic Sci. Lett.,* **2,** 148–152.

——, and A. Sundfjord, 2007: Observations of upper ocean boundary layer dynamics in the marginal ice zone. *J. Geophys. Res.,* **112,** C04012, doi:10.1029/2005JC003428.

——, R. Skogseth, and F. Geyer, 2010: Internal waves and mixing in the marginal ice zone near the Yermak Plateau. *J. Phys. Oceanogr.,* **40,** 1613–1630.

Furevik, T., and A. Foldvik, 1996: Stability at M_2 critical latitude in the Barents Sea. *J. Geophys. Res.,* **101** (C4), 8823–8838.

Holloway, G., and A. Proshutinsky, 2007: Role of tides in Arctic ocean/ice climate. *J. Geophys. Res.,* **112,** C04S06, doi:10.1029/2006JC003643.

Itoh, M., E. Carmack, K. Shimada, F. McLaughlin, S. Nishino, and S. Zimmerman, 2007: Formation and spreading of Eurasian source oxygen-rich halocline water into the Canadian Basin in the Arctic Ocean. *Geophys. Res. Lett.,* **34,** L08603, doi:10.1029/2007GL029482.

Jakobsson, M., N. Cherkis, J. Woodward, B. Coakley, and R. Macnab, 2000: A new grid of Arctic bathymetry: A significant resource for scientists and mapmakers. *Eos, Trans. Amer. Geophys. Union,* **81,** 89–96.

Kelley, D. E., H. Fernando, A. Gargett, J. Tanny, and E. Oezsoy, 2003: The diffusive regime of double-diffusive convection. *Prog. Oceanogr.,* **56,** 461–481.

Kowalik, Z., and A. Proshutinsky, 1994: The Arctic Ocean tides. *The Polar Oceans and Their Role in Shaping the Global Environment, Geophys. Monogr.,* Vol. 85, Amer. Geophys. Union, 137–158.

Lenn, Y. D., and Coauthors, 2009: Vertical mixing at intermediate depths in the arctic boundary current. *Geophys. Res. Lett.,* **36,** L05601, doi:10.1029/2008GL036792.

Liu, P. C., 1994: Wavelet spectrum analysis and ocean wind waves. *Wavelets in Geophysics,* E. Foufoula-Georgiou and P. Kumar, Eds., Vol. 4, Academic Press, 151–166.

Mackinnon, J. A., and M. C. Gregg, 2005: Near-inertial waves on the New England shelf: The role of evolving stratification, turbulent dissipation, and bottom drag. *J. Phys. Oceanogr.,* **35,** 2408–2424.

Makinson, K., 2002: Modeling tidal current profiles and vertical mixing beneath Filchner Ronne Ice Shelf, Antarctica. *J. Phys. Oceanogr.,* **32,** 202–215.

——, M. Schröder, and S. Østerhus, 2006: Effect of critical latitude and seasonal stratification on tidal current profiles along Ronne Ice Front, Antarctica. *J. Geophys. Res.,* **111,** C03022, doi:10.1029/2005JC003062.

Maykut, G. A., and N. Untersteiner, 1971: Some results from a time-dependent thermodynamic model of sea ice. *J. Geophys. Res.,* **76,** 1550–1575.

McPhee, M. G., 1992: Turbulent heat flux in the upper ocean under sea ice. *J. Geophys. Res.,* **97** (C4), 5365–5379.

——, 2002: Turbulent stress at the ice/ocean interface and bottom surface hydraulic roughness during the SHEBA drift. *J. Geophys. Res.,* **107,** 8037, doi:10.1029/2000JC000633.

——, and D. G. Martinson, 1994: Turbulent mixing under drifting pack ice in the Weddell Sea. *Science,* **263,** 218–221.

——, T. Kikuchi, J. H. Morison, and T. P. Stanton, 2003: Ocean-to-ice heat flux at the North Pole environmental observatory. *Geophys. Res. Lett.,* **30,** 2274, doi:10.1029/2003GL018580.

——, R. Kwok, R. Robins, and M. Coon, 2005: Upwelling of Arctic pycnocline associated with shear motion of sea ice. *Geophys. Res. Lett.,* **32,** L10616, doi:10.1029/2004GL021819.

Meincke, J., B. Rudels, and H. J. Friedrich, 1997: The Arctic Ocean–Nordic Seas thermohaline system. *ICES J. Mar. Sci.,* **54,** 283–299.

Morozov, E. G., V. T. Paka, and V. V. Bakhanov, 2008: Strong internal tides in the Kara Gates Strait. *Geophys. Res. Lett.,* **35,** L16603, doi:10.1029/2008GL033804.

Osborn, T., 1980: Estimates of the local rate of vertical diffusion from dissipation measurements. *J. Phys. Oceanogr.,* **10,** 83–89.

Padman, L., 1995: Small scale physical process in the Arctic Ocean. *Arctic Oceanography, Marginal Ice Zones and Continental Shelves, Geophys. Monogr.,* Vol. 49, Amer. Geophys. Union, 97–129.

——, and T. M. Dillon, 1987: Vertical heat fluxes through the Beaufort Sea thermohaline staircase. *J. Geophys. Res.,* **92,** 10 799–10 806.

——, and ——, 1991: Turbulent mixing near the Yermak Plateau during the Coordinated Eastern Arctic Experiment. *J. Geophys. Res.,* **96,** 4769–4782.

——, and S. L. Erofeeva, 2004: A barotropic tidal model for the Arctic Ocean. *Geophys. Res. Lett.,* **31,** L02303, doi:10.1029/2003GL019003.

——, A. Plueddemann, R. Muench, and R. Pinkel, 1992: Diurnal tides near the Yermak Plateau. *J. Geophys. Res.,* **97** (C8), 12 639–12 652.

——, S. L. Howard, A. H. Orsi, and R. D. Muench, 2009: Tides of the northwestern Ross Sea and their impact on dense outflows of Antarctic Bottom Water. *Deep-Sea Res. II,* **56,** 818–834.

Pawlowicz, R., B. Beardsley, and S. Lentz, 2002: Classical tidal harmonic analysis including error estimates in MATLAB using T_TIDE. *Comput. Geosci.,* **28,** 929–937.

Prandle, D., 1982: The vertical structure of tidal currents and other oscillatory flows. *Cont. Shelf Res.,* **1,** 191–207.

Prinsenberg, S. J., and E. B. Bennett, 1989: Vertical variations of tidal currents in shallow land fast ice-covered regions. *J. Phys. Oceanogr.,* **19,** 1268–1278.

Rainville, L., and P. Winsor, 2008: Mixing across the Arctic Ocean: Microstructure observations during the Beringia 2005 expedition. *Geophys. Res. Lett.,* **35,** L08606, doi:10.1029/2008GL033532.

——, and R. A. Woodgate, 2009: Observations of internal wave generation in the seasonally ice-free Arctic. *Geophys. Res. Lett.,* **36,** L23604, doi:10.1029/2009GL041291.

Rippeth, T. P., 2005: Mixing in seasonally stratified shelf seas: A shifting paradigm. *Philos. Trans. Roy. Soc. London,* **363A,** 2837–2854.

——, J. H. Simpson, and E. Williams, 2003: Measurement of the rates of production and dissipation of turbulent kinetic energy in an energetic tidal flow: Red Wharf Bay revisited. *J. Phys. Oceanogr.,* **33,** 1889–1901.

——, P. Wiles, M. R. Palmer, J. Sharples, and J. Tweddle, 2009: The diapycnal nutrient flux and shear-induced diapycnal mixing in the seasonally stratified western Irish Sea. *Cont. Shelf Res.,* **29,** 1580–1587.

Rudels, B., L. Anderson, and E. Jones, 1996: Formation and evolution of the surface mixed layer and halocline of the Arctic Ocean. *J. Geophys. Res.,* **101** (C4), 8807–8821.

——, R. D. Muench, J. Gunn, U. Schauer, and H. J. Freidrich, 2000: Evolution of the Arctic boundary current north of the Siberian shelves. *J. Mar. Syst.,* **25,** 77–99.

Shimada, K., M. Itoh, S. Nishino, F. McLaughlin, E. Carmack, and A. Proshutinsky, 2005: Halocline structure in the Canadian Basin of the Arctic Ocean. *Geophys. Res. Lett.,* **32,** L03605, doi:10.1029/2004GL021358.

Simpson, J. H., and J. P. Tinker, 2009: A test of the influence of tidal stream polarity on the structure of turbulent dissipation. *Cont. Shelf Res.,* **29,** 320–332.

——, W. R. Crawford, T. P. Rippeth, A. R. Campbell, and J. V. S. Cheok, 1996: The vertical structure of turbulent dissipation in shelf seas. *J. Phys. Oceanogr.,* **26,** 1579–1590.

Sirevaag, A., and I. Fer, 2009: Early spring oceanic heat fluxes and mixing observed from drift stations north of Svalbard. *J. Phys. Oceanogr.,* **39,** 3049–3069.

Sundfjord, A., I. Fer, Y. Kasajima, and H. Svendsen, 2007: Observations of turbulent mixing and hydrography in the marginal ice zone of the Barents Sea. *J. Geophys. Res.,* **112,** C05008, doi:10.1029/2006JC003524.

Turner, J. S., 2010: The melting of ice in the Arctic Ocean: The influence of double-diffusive transport of heat from below. *J. Phys. Oceanogr.,* **40,** 249–256.

Woodgate, R. A., K. Aagaard, J. H. Swift, K. K. Falkner, and W. M. Smethie Jr., 2005: Pacific ventilation of the Arctic Ocean's lower halocline by upwelling and diapycnal mixing over the continental margin. *Geophys. Res. Lett.,* **32,** L18609, doi:10.1029/2005GL023999.